

# Cancer Research

## Interstitial Fluid Pressure and Associated Lymph Node Metastasis Revealed in Tumors by Dynamic Contrast-Enhanced MRI

Tord Hompland, Christine Ellingsen, Kirsti Marie Øvrebø, et al.

*Cancer Res* 2012;72:4899-4908. Published online September 30, 2012.

**Updated Version** Access the most recent version of this article at:  
doi:[10.1158/0008-5472.CAN-12-0903](https://doi.org/10.1158/0008-5472.CAN-12-0903)

**Supplementary Material** Access the most recent supplemental material at:  
<http://cancerres.aacrjournals.org/content/suppl/2012/09/28/72.19.4899.DC1.html>

**Cited Articles** This article cites 45 articles, 15 of which you can access for free at:  
<http://cancerres.aacrjournals.org/content/72/19/4899.full.html#ref-list-1>

**E-mail alerts** [Sign up to receive free email-alerts](#) related to this article or journal.

**Reprints and Subscriptions** To order reprints of this article or to subscribe to the journal, contact the AACR Publications Department at [pubs@aacr.org](mailto:pubs@aacr.org).

**Permissions** To request permission to re-use all or part of this article, contact the AACR Publications Department at [permissions@aacr.org](mailto:permissions@aacr.org).

## Interstitial Fluid Pressure and Associated Lymph Node Metastasis Revealed in Tumors by Dynamic Contrast-Enhanced MRI

Tord Hompland, Christine Ellingsen, Kirsti Marie Øvrebø, and Einar K. Rofstad

### Abstract

Elevated interstitial fluid pressure (IFP) in tumors can cause metastatic dissemination and treatment resistance, but its study poses a challenge because of a paucity of noninvasive imaging strategies. In this study, we address this issue by reporting the development of a noninvasive tool to assess tumor IFP and interstitial hypertension-induced lymph node metastasis. Using mouse xenograft models of several types of human cancer, we used gadolinium diethylene-triamine penta-acetic acid (Gd-DTPA) as a contrast agent for dynamic contrast-enhanced MRI (DCE-MRI). Immediately after Gd-DTPA administration, a high-signal-intensity rim was observed in the tumor periphery, which moved outward with time. Assuming the velocity of Gd-DTPA to be equal to the fluid flow velocity, we used a simple model of peritumoral interstitial fluid flow to calculate the fluid flow velocity at the tumor surface ( $v_0$ ) based on the rim movement. Significant positive correlations were found between  $v_0$  and IFP in all tumor xenografts. Moreover, the primary tumors of metastasis-positive mice displayed higher IFP and  $v_0$  than the primary tumors of metastasis-negative mice. Findings were confirmed in cervical cancer patients with pelvic lymph node metastases, where we found  $v_0$  to be higher compared with patients without lymph node involvement ( $P < 0.00001$ ). Together, these findings establish that Gd-DTPA-based DCE-MRI can noninvasively visualize tumor IFP, and they reveal the potential for  $v_0$  determined by this method to serve as a novel general biomarker of tumor aggressiveness. *Cancer Res*; 72(19); 4899–908. ©2012 AACR.

### Introduction

Malignant solid tumors generally have a higher interstitial fluid pressure (IFP) than normal tissues (1–3). Tumor tissues develop interstitial hypertension because they show high resistance to blood flow, low resistance to transcapillary fluid flow, and impaired lymphatic drainage (1, 3). The microvascular hydrostatic pressure is the principal driving force for the elevated IFP of tumors (4). Fluid is forced from the microvasculature into the interstitium where it accumulates, distends the extracellular matrix, and causes interstitial hypertension (1, 4). A pseudostable state is established with uniformly elevated IFP throughout the tumor tissue except close to the surface, where the IFP drops steeply to normal tissue values (5, 6). Because of the steep IFP gradient at the tumor surface, fluid oozes out from the tumor tissue into the surrounding normal tissue, where it is collected by functional lymphatics (7).

Experimental and clinical studies have provided substantial evidence that high IFP in tumors is a significant therapeutic problem (1–3). First, high IFP may cause low and heterogeneous uptake of chemical therapeutic agents, leading to resistance to chemotherapy, immunotherapy, and some forms of gene therapy (3, 4). Second, interstitial hypertension may cause resistance to radiation therapy. Studies of melanoma xenografts have shown that high IFP may be linked to poor radio-curability through hypoxia-dependent as well as hypoxia-independent mechanisms (8, 9). Third, high IFP may promote metastatic spread. The incidence of pulmonary and lymph node metastases has been shown to be associated with the IFP of the primary tumor in mice bearing melanoma and cervical carcinoma xenografts (10, 11). Fourth, the IFP of the primary tumor has been shown to be an independent prognostic parameter for patients with locally advanced cervical carcinoma (12–14). In these studies, high-tumor IFP was associated with poor disease-free survival independent of conventional prognostic factors, such as tumor size, stage, and lymph node status (13, 14).

An imaging method for noninvasive assessment of the IFP of tumors is needed to evaluate the potential of IFP as a biomarker for cancer aggressiveness. The possibility of using dynamic contrast-enhanced MRI (DCE-MRI) has been explored in a limited number of studies. Using a protocol based on slow infusion of gadolinium diethylene-triamine penta-acetic acid (Gd-DTPA), Hassid and colleagues showed that parametric images of the steady-state concentration of

**Authors' Affiliation:** Group of Radiation Biology and Tumor Physiology, Department of Radiation Biology, Institute for Cancer Research, Oslo University Hospital, Oslo, Norway

**Note:** Supplementary data for this article are available at Cancer Research Online (<http://cancerres.aacrjournals.org/>).

**Corresponding Author:** Einar K. Rofstad, Department of Radiation Biology, Institute for Cancer Research, Norwegian Radium Hospital, Box 4953 Nydalen, 0424 Oslo, Norway. Phone: 47-2278-1206; Fax: 47-2278-1207; E-mail: [einark.rofstad@rr-research.no](mailto:einark.rofstad@rr-research.no)

doi: 10.1158/0008-5472.CAN-12-0903

©2012 American Association for Cancer Research.

Gd-DTPA reflected the spatial distribution of the IFP of xenografted tumors, but correlations between steady-state Gd-DTPA concentration and IFP were not reported (15). Gulliksrud and colleagues reported significant correlations between  $E \cdot F$  ( $E$  is the initial extraction fraction of Gd-DTPA and  $F$  is blood perfusion) and IFP in melanoma xenografts, but  $E \cdot F$  decreased with increasing IFP in intradermal tumors and increased with increasing IFP in intramuscular tumors (16, 17). In a study of cervical carcinoma patients, Haider and colleagues found significant correlations between DCE-MRI-derived parameters and IFP, but the correlations were too weak to be clinically useful (18). All these attempts to determine IFP by DCE-MRI were based on assessment of parameters related to the efficiency of vascular delivery and transcapillary transfer of Gd-DTPA.

However, there is significant theoretical evidence that DCE-MRI parameters related to the washout of Gd-DTPA at the tumor surface may provide information on the IFP of tumors (19). This possibility was investigated in the work reported here. Our study was based on the hypothesis that the velocity of the fluid flow from tumors into adjacent normal tissues is determined by the IFP drop at the tumor surface. Moreover, in accordance with previous suggestions (10, 19–21), we hypothesized that the development of lymph node metastases is associated with the fluid flow out of tumors as the fluid may direct tumor-secreted lymphangiogenic factors and other metastasis-promoting chemokines toward peritumoral lymphatics. To test these hypotheses, the Gd-DTPA velocity at the tumor surface was assessed by DCE-MRI in xenografted tumors and human cervical carcinomas. Strong correlations were found between Gd-DTPA velocity, tumor IFP, and incidence of lymph node metastases in melanoma and cervical carcinoma xenografts. Moreover, the Gd-DTPA velocity at the primary tumor surface discriminated well between cervical carcinoma patients with and without pelvic lymph node metastases.

## Materials and Methods

### Preclinical experiments

The TS-415 human cervical carcinoma and the U-25 human melanoma cell lines were established and characterized in our laboratory, and a large stock of cells were frozen and stored in liquid nitrogen (22, 23). The cells used in the present experiments were obtained from our frozen stock and were maintained in monolayer culture in RPMI 1640 supplemented with 13% bovine calf serum, 250 mg/L penicillin, and 50 mg/L streptomycin. Xenografted tumors were initiated by inoculating  $5.0 \times 10^5$  cells into the gastrocnemius muscle of adult female BALB/c *nu/nu* mice. The mice were maintained under specific pathogen-free conditions and, unless otherwise stated, they were subjected to DCE-MRI when the tumor was approximately 500 mm<sup>3</sup>. Tumor IFP was measured immediately after the DCE-MRI, and the mice were then euthanized and examined for lymph node metastases. The mice were anesthetized with fentanyl citrate (0.63 mg/kg), fluanisone (20 mg/kg), and midazolam (10 mg/kg) before the DCE-MRI.

The DCE-MRI was carried out as described previously (24, 25). Gd-DTPA (Magnevist; Schering) with a molecular weight of

0.55 kDa or gadomelitol (Vistarem; Guerbet) with a molecular weight of 6.5 kDa was used as contrast agent. The contrast agents were diluted in 0.9% saline to a final concentration of 60 mmol/L (Gd-DTPA) or 7.0 mmol/L (gadomelitol) and were administered in the tail vein in a bolus dose of 5.0 mL/kg.  $T_1$ -weighted images (TR = 200 ms, TE = 3.5 ms, and  $\alpha_{TI} = 80^\circ$ ) were recorded at a spatial resolution of  $0.23 \times 0.23 \times 2.0$  mm<sup>3</sup> and a time resolution of 14 seconds with a 1.5-T whole-body scanner (Signa; General Electric) and a slotted tube resonator transceiver mouse coil. The coil was insulated with styrofoam to prevent excessive heat loss from the mice. The body core temperature of the mice was kept at 37°C to 38°C during imaging with a thermostat-regulated heating pad. The tumors were imaged axially in a single section through the center by using an image matrix of  $256 \times 128$ , a field of view of  $6 \times 3$  cm<sup>2</sup>, and one excitation. Three  $T_1$ -weighted images were acquired before contrast was administered, and  $T_1$ -weighted images were recorded for 15 minutes after the contrast administration.  $T_2$ -weighted images were acquired immediately before the  $T_1$ -weighted series by using a spin echo sequence (TR = 3000 ms, TE = 65 ms). Signal intensity images were generated with the SigmaPlot software (SPSS Science).

IFP was measured in the center of the tumors with a Millar SPC 320 catheter equipped with a Mikro-Tip transducer with diameter 0.66 mm (Millar Instruments; 26). Marks on the catheter assured correct positioning of the sensor, and a single measurement was carried out in each tumor. The catheter was connected to a computer via a Millar TC-510 control unit and a preamplifier, and the LabVIEW software (National Instruments) was used for data acquisition. By measuring the IFP in the same tumors twice, we have shown that this method produces highly reproducible IFP values (16).

The mice were euthanized immediately after the IFP measurement and examined for external lymph node metastases in the inguinal, axillary, interscapular, and submandibular regions and internal lymph node metastases in the abdomen and mediastinum. The presence of metastatic growth in enlarged lymph nodes was confirmed by histologic examination (27).

The study was approved by the Institutional Committee on Research Animal Care and was carried out according to the USPHS Policy on Humane Care and Use of Laboratory Animals.

### Clinical investigations

Fifty patients with locally advanced squamous cell carcinoma of the uterine cervix subjected to DCE-MRI at the Norwegian Radium Hospital were selected for this study from a cohort of 60 consecutive patients. Only patients showing significant image distortions caused by bowel or bladder movements during the imaging were excluded from analysis.

The imaging was carried out with a 1.5-T whole-body scanner (Signa; General Electric) and a 4-channel phased-array surface coil. Before the DCE-MRI, the entire pelvic region was scanned with an axial  $T_2$ -weighted fast spin echo sequence (TR = 4960 ms, TE = 84 ms, image matrix:  $512 \times 512$ , field of view:  $20 \times 20$  cm<sup>2</sup>, number of excitations: 1.5, slice thickness: 5 mm, slice spacing: 6 mm). The DCE-MRI was carried out at a temporal resolution of 29 seconds by using an axial  $T_1$ -

weighted spoiled gradient recalled sequence (TR = 160 ms, TE = 3.5 ms,  $\alpha_{TI} = 90^\circ$ , image matrix:  $256 \times 256$ , field of view:  $20 \times 20$  cm<sup>2</sup>, number of excitations: 1, slice thickness: 5 mm, slice spacing: 6 mm). Three  $T_1$ -weighted images were acquired before a bolus dose of 0.1 mmol/kg Gd-DTPA was administered, and  $T_1$ -weighted images were recorded for 10 minutes after the Gd-DTPA administration.

Primary tumor volume and metastatic status were determined by examining MR images in the open source dicom viewer Osirix (28). A region of interest (ROI) encompassing the tumor area was drawn in each  $T_2$ -weighted image, and tumor volume was reconstructed and calculated from these ROIs with a built-in function of Osirix. Metastatic status was assessed by examining the internal, external, and lower common iliac chains. A lymph node was scored as metastasis-positive when its shortest diameter in the  $T_2$ -weighted images was longer than 1.0 cm and the  $T_1$ -weighted images showed a contrast enhancement pattern similar to that of the primary tumor.

The investigations were approved by the institutional review board and were conducted in accordance with the Declaration of Helsinki. Informed consent was obtained from each patient.

### Immunohistochemistry

Histologic sections were immunostained for blood vessels or connective tissue by using a peroxidase-based indirect staining method (29). An anti-mouse CD31 rat monoclonal antibody (Research Diagnostics) or an anticollagen rabbit polyclonal antibody (Dako) was used as primary antibody.

### Statistical analysis

Curves were fitted to data by regression analysis. The Pearson product moment correlation test was used to search for correlations between parameters. Statistical comparisons of data were carried out with the Student  $t$  test when the data complied with the conditions of normality and equal variance. Under other conditions, comparisons were carried out by nonparametric analysis using the Mann-Whitney rank-sum test. Probability values of  $P < 0.05$ , determined from 2-sided tests, were considered significant. The statistical analysis was conducted by using the SigmaStat statistical software (SPSS Science).

### Model for the peritumoral interstitial fluid flow of tumors

Fluid convection in tumor tissues is proportional to the local IFP gradient,  $dP/dx$ , and can be described by Darcy's law,  $v = -K \cdot dP/dx$ , where  $K$  is the hydraulic conductivity of the tissue and  $v$  is the fluid flow velocity. We assume a model where the IFP is homogeneously elevated throughout the tissue ( $P = P_0$ ) except close to the surface, where it drops steeply to normal tissue values (Fig. 1). This model is in agreement with IFP profiles measured in tumors in mice (5, 10). According to Darcy's law, there is fluid convection only at the tumor surface in this model, from the tumor periphery into the surrounding normal tissue, and no convection inside the tumor. Moreover, we assume that the fluid flow is attenuated linearly with the distance from the tumor surface. Thus, the fluid flow velocity at a distance  $S$  from the tumor surface,  $v(S)$ , can be described by

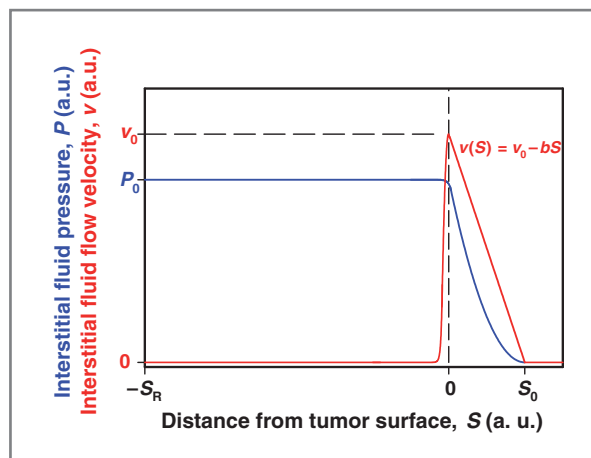


**Figure 1.** The figure shows how the IFP ( $P$ , blue curve) and the interstitial fluid flow velocity ( $v$ , red curve) vary radially in tumors (i.e., with  $S$ , the distance from the tumor surface) in our model. The IFP is uniformly elevated ( $P = P_0$ ) from the tumor center ( $S = -S_R$ ) to the tumor surface ( $S = 0$ ), where it drops steeply and reaches the IFP of the surrounding normal tissue at  $S = S_0$ . There is no convection between the tumor center and the tumor surface ( $v = 0$ ). The convection increases abruptly at the tumor surface, where the interstitial fluid flow velocity reaches its maximum value ( $v = v_0$ ). From the tumor surface, the interstitial fluid flow velocity declines linearly with the distance into the surrounding normal tissue ( $v = v_0 - bS$ , where  $b$  is the attenuation coefficient) and reaches zero at  $S = S_0$  and, thus, there is no convection ( $v = 0$ ) at distances beyond  $S_0$ . a. u., arbitrary units.

the expression  $v(S) = v_0 - bS$ , where  $v_0$  is the velocity at the tumor surface and  $b$  is the attenuation coefficient (Fig. 1). Using the definition of velocity,  $v = dS/dt$ , and integrating this equation, we have  $S(t) = S_0 \cdot (1 - e^{-bt})$ , where  $S_0 = v_0/b$  represents the maximum distance the fluid can flow from the tumor surface. Thus, the fluid flow velocity reaches zero at  $S_0$ , and beyond  $S_0$ , we have  $v = 0$  (Fig. 1).

## Results

### Peritumoral flow of Gd-DTPA

To illustrate the peritumoral flow of Gd-DTPA in xenografted tumors, we report representative data by using TS-415 tumors as examples. The tumors showed a band of connective tissue in the periphery, and the vessel density within this band was high relative to that in the central tumor regions (Fig. 2A). The  $T_1$ -weighted image recorded immediately after the Gd-DTPA administration showed a high-signal-intensity rim in the tumor periphery, corresponding to the position of the band of highly vascularized connective tissue (Fig. 2B). The high-signal-intensity rim moved outward with time, as illustrated in Supplementary Movie S1 and by marked still frames from this movie in Fig. 2B. The rim movement was quantified by assuming that the flow of Gd-DTPA complied with the model for peritumoral interstitial fluid flow described above. Correct quantification of the rim movement required that the tumors did not move during the DCE-MRI, as was verified by examining the position of the tumors relative to the coordinates of the image matrix (Fig. 2B). To quantify the rim movement, we measured the signal intensity across the rim at different time points after the administration of Gd-DTPA (Fig.

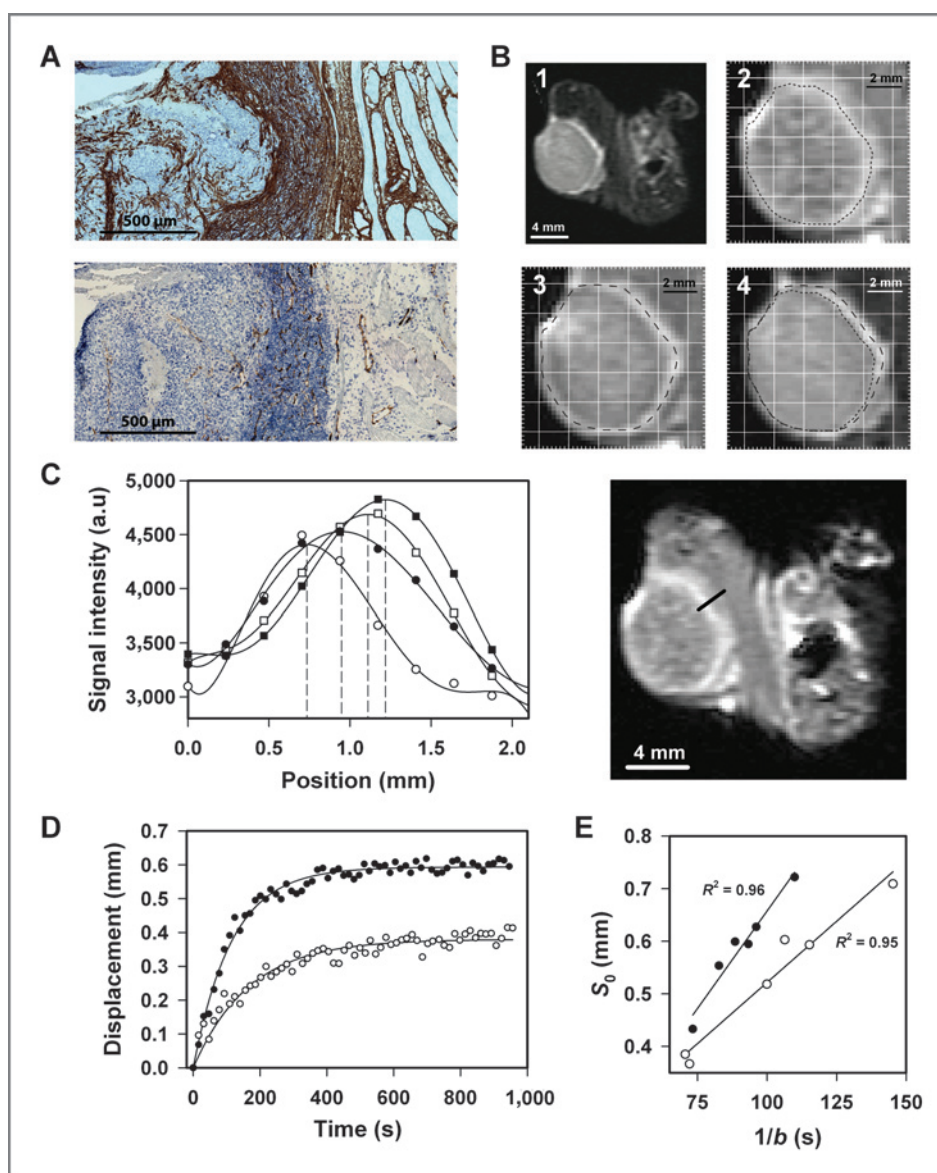


**Figure 2.** The figure shows representative data for the TS-415 cervical carcinoma xenograft line. A, immunohistochemical preparations stained with an anticollagen antibody to visualize connective tissue (top) or an anti-CD31 antibody to visualize blood vessels (bottom). B,  $T_2$ -weighted images of a tumor recorded before Gd-DTPA administration (images 1 and 4) and  $T_1$ -weighted images recorded after Gd-DTPA administration (images 2 and 3) showing a high-signal-intensity rim in the tumor periphery. The dashed contour lines show the position of the rim approximately 15 seconds (image 2) and approximately 10 minutes (image 3) after the Gd-DTPA administration. The contour lines are superimposed on the  $T_2$ -weighted image (image 4), showing that the high-signal-intensity rim moved outward with time. The outward movement can be followed in detail in Supplementary Movie S1. C, plots referring to the same tumor as in B showing the variation in signal intensity across the tumor periphery approximately 15 seconds ( $\circ$ ), approximately 80 seconds ( $\bullet$ ), approximately 110 seconds ( $\square$ ), and approximately 450 seconds ( $\blacksquare$ ) after the Gd-DTPA administration. The points refer to signal intensities calculated from four neighboring pixels by bilinear interpolation. The curves represent the best fits of a polynomial of the 6th degree. The dashed vertical lines indicate the position of the peak signal intensity at the different time points and, hence, the position of the high-signal-intensity rim. The origin of the abscissa (position zero) is an arbitrarily selected pixel of the image matrix. The data (left) refer to the black line in the  $T_1$ -weighted image (right). D, plots showing the displacement of the high-signal-intensity rim versus time for a tumor with low IFP ( $\circ$ ) and a tumor with high IFP ( $\bullet$ ). The origin (displacement zero and time zero) refers to the first  $T_1$ -weighted image recorded after the Gd-DTPA administration. There is one point for each time frame of the DCE-MRI series. The curves show the best fits of  $S(t) = S_0(1 - e^{-bt})$ , where  $S$  represents displacement and  $t$  represents time. E, plots of  $S_0$  versus  $1/b$  for a tumor with low IFP ( $\circ$ ) and a tumor with high IFP ( $\bullet$ ). Plots similar to those in D were established for 6 different positions in the tumor periphery, and  $S_0$  and  $b$  were calculated from the best curve fits of  $S(t) = S_0(1 - e^{-bt})$ . Linear curves were fitted to the data by regression analysis, giving correlation coefficients of  $R^2 = 0.95$  and  $0.96$ . The slopes of the curves represent the flow velocity at the tumor surface ( $S_0 \cdot b = v_0$ ). a. u., arbitrary units; s, seconds.

2C), calculated the displacement of the rim from the position of the peak signal intensity, plotted rim displacement versus time, and calculated  $S_0$ ,  $v_0$ , and  $b$  from the best curve fits of  $S(t) =$

$S_0(1 - e^{-bt})$  (Fig. 2D). The maximum rim displacement varied around the tumor periphery (Fig. 2B). To investigate whether also the initial flow velocity varied around the periphery,  $S_0$ ,  $v_0$ ,

and  $b$  were determined in 6 different positions in the tumor periphery. In contrast to  $S_0$ ,  $\nu_0$  did not vary around the periphery. This is illustrated in Fig. 2E, which shows that plots of  $S_0$  versus  $1/b$  were well fitted by linear curves (i.e., curves with a constant slope  $\nu_0 = S_0 \cdot b$ ).

The peritumoral flow of Gd-DTPA in human cervical carcinomas was similar to that in the xenografted tumors, as illustrated in Supplementary Movie S2. The movie shows a representative example and refers to a patient with a large primary tumor and metastatic growth in several pelvic lymph nodes. Marked still frames from the movie are presented in Fig. 3A, and Fig. 3B shows plots of the rim displacement versus time

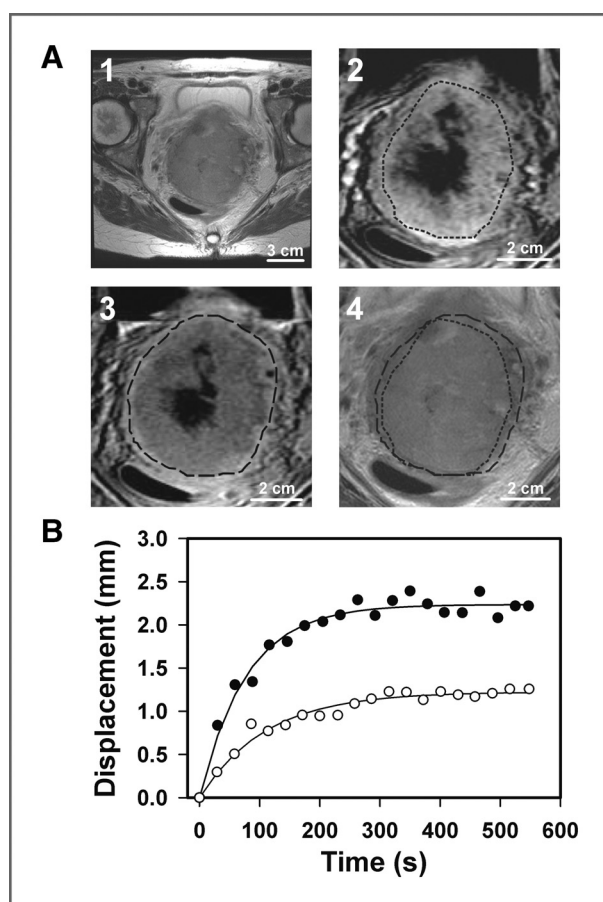


Figure 3. A,  $T_2$ -weighted images of a human cervical carcinoma recorded before Gd-DTPA administration (images 1 and 4) and  $T_1$ -weighted images of the tumor recorded after Gd-DTPA administration (images 2 and 3) showing a high-signal-intensity rim in the periphery. The dashed contour lines show the position of the rim approximately 30 seconds (image 2) and approximately 10 minutes (image 3) after the Gd-DTPA administration. The contour lines are superimposed on the  $T_2$ -weighted image (image 4), showing that the high-signal-intensity rim moved outward with time. The outward movement can be followed in detail in Supplementary Movie S2. B, plots showing the displacement of the high-signal-intensity rim versus time for 2 patients, one without (○) and the other with (●) lymph node metastases. The origin (displacement zero and time zero) refers to the first  $T_1$ -weighted image recorded after the Gd-DTPA administration. There is one point for each time frame of the DCE-MRI series. The curves show the best fits of  $S(t) = S_0 \cdot (1 - e^{-bt})$ , where  $S$  represents displacement and  $t$  represents time, s, seconds.

for this patient and a patient without pelvic lymph node involvement. As for the xenografted tumors,  $S_0$ ,  $\nu_0$ , and  $b$  were calculated from the best curve fits of  $S(t) = S_0 \cdot (1 - e^{-bt})$ .

### $S_0$ , $b$ , and $\nu_0$ were positively correlated to IFP in TS-415 and U-25 xenografts

Thirty-six TS-415 tumors and 29 U-25 tumors were subjected to Gd-DTPA-based DCE-MRI and subsequent measurement of IFP. Significant correlations were found between  $S_0$ ,  $b$ , and  $\nu_0$  on the one hand and IFP on the other, both for TS-415 (Fig. 4A) and U-25 (Fig. 4B) tumors. The correlation with IFP was particularly strong for  $\nu_0$ . The data for the TS-415 and U-25 tumors are plotted together in Fig. 4C, illustrating that nearly identical correlations were obtained for the 2 xenograft lines. Furthermore, 14 TS-415 tumors and 10 U-25 tumors were subjected to DCE-MRI with gadomelitol as contrast agent.  $\nu_0$  increased with increasing IFP, both in TS-415 (Fig. 5A) and U-25 (Fig. 5B) tumors. The correlations between  $\nu_0$  and IFP were similar for the 2 tumor lines and similar to those obtained with Gd-DTPA (Fig. 5C).

### There was no association between IFP or $\nu_0$ and tumor size in TS-415 and U-25 xenografts

Twelve tumors of each line differing in volume from approximately 300 mm<sup>3</sup> to approximately 1,000 mm<sup>3</sup> were subjected to Gd-DTPA-based DCE-MRI and measurement of IFP. Significant correlation between IFP and tumor size or  $\nu_0$  and tumor size was not found in any of the lines (Supplementary Fig. S1).

### High IFP and high $\nu_0$ were associated with lymph node metastasis in TS-415 and U-25 xenografts

Sixteen mice bearing TS-415 tumors and 24 mice bearing U-25 tumors were autopsied and examined for lymph node metastases after Gd-DTPA-based DCE-MRI and IFP measurement. Metastases were found in 7 mice with TS-415 tumors and 11 mice with U-25 tumors, whereas the other mice were metastasis-negative. In the TS-415 line, the primary tumors of the metastasis-positive mice showed significantly higher IFP and significantly higher  $\nu_0$  than those of the metastasis-negative mice (Fig. 6A). In the U-25 line, both IFP,  $S_0$ ,  $b$ , and  $\nu_0$  were significantly higher in the metastatic than in the nonmetastatic primary tumors (Fig. 6B).

### Large tumor volume and high values of $b$ and $\nu_0$ were associated with pelvic lymph node metastasis in human cervical carcinoma

Fifty cervical carcinoma patients subjected to  $T_2$ -weighted MRI and DCE-MRI of the pelvis were included in the study. Positive lymph nodes were detected in 27 patients, whereas the other 23 patients did not show evidence of metastatic growth. The primary tumors were larger in the metastasis-positive patients than in the patients without metastatic deposits (Fig. 7A).  $S_0$  did not differ between the patients with and the patients without positive lymph nodes (Fig. 7B). On the other hand, the metastatic tumors differed from the nonmetastatic tumors by showing significantly higher values for both  $b$  (Fig. 7C) and  $\nu_0$  (Fig. 7D).

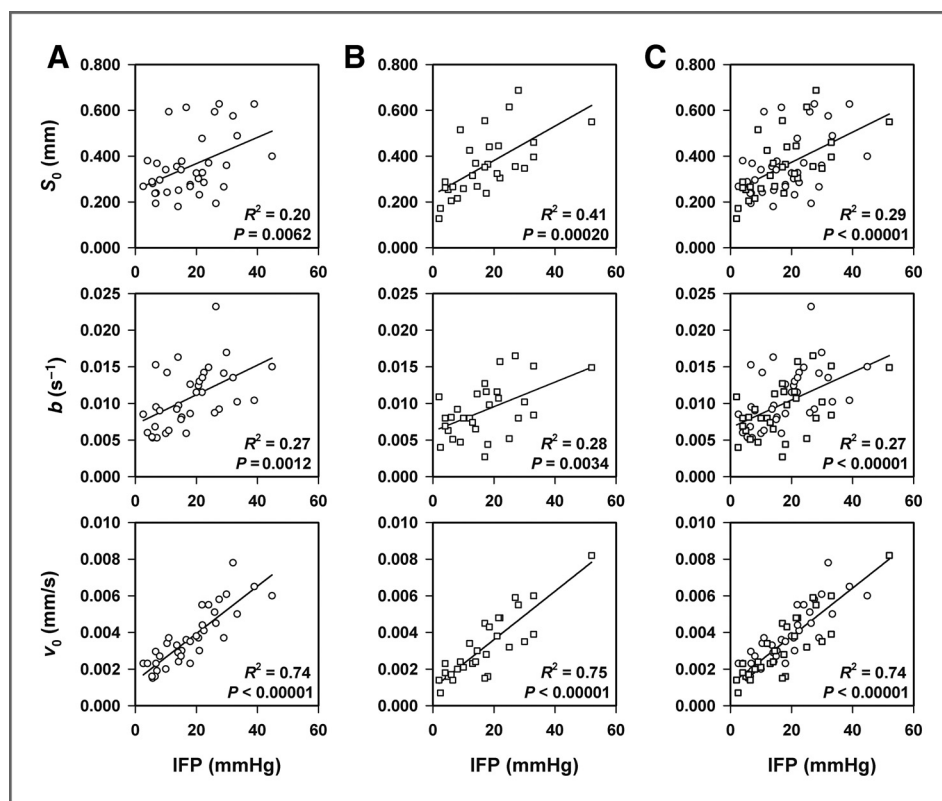


**Figure 4.**  $S_0$ ,  $b$ , and  $v_0$  versus IFP for TS-415 tumors (A), U-25 tumors (B), and TS-415 and U-25 tumors plotted together (C). Gd-DTPA was used as contrast agent. Symbols represent single TS-415 ( $\circ$ ) and U-25 ( $\square$ ) tumors. Curves were fitted to the data by linear regression analysis.  $R^2$  and  $P$  values were determined by the Pearson product moment correlation test. s, seconds.

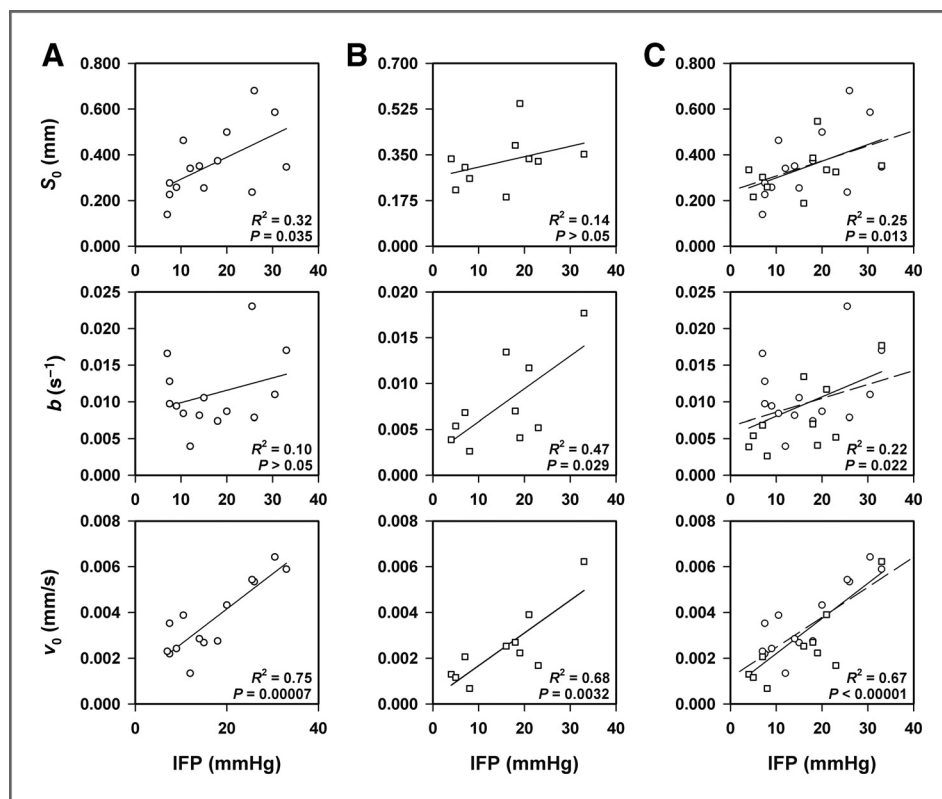


**Figure 5.**  $S_0$ ,  $b$ , and  $v_0$  versus IFP for TS-415 tumors (A), U-25 tumors (B), and TS-415 and U-25 tumors plotted together (C). Gadomelitol was used as contrast agent. Symbols represent single TS-415 ( $\circ$ ) and U-25 ( $\square$ ) tumors. Solid curves were fitted to the data by linear regression analysis. Dashed curves were redrawn from Fig. 4 and refer to data obtained with Gd-DTPA.  $R^2$  and  $P$  values were determined by the Pearson product moment correlation test. s, seconds.

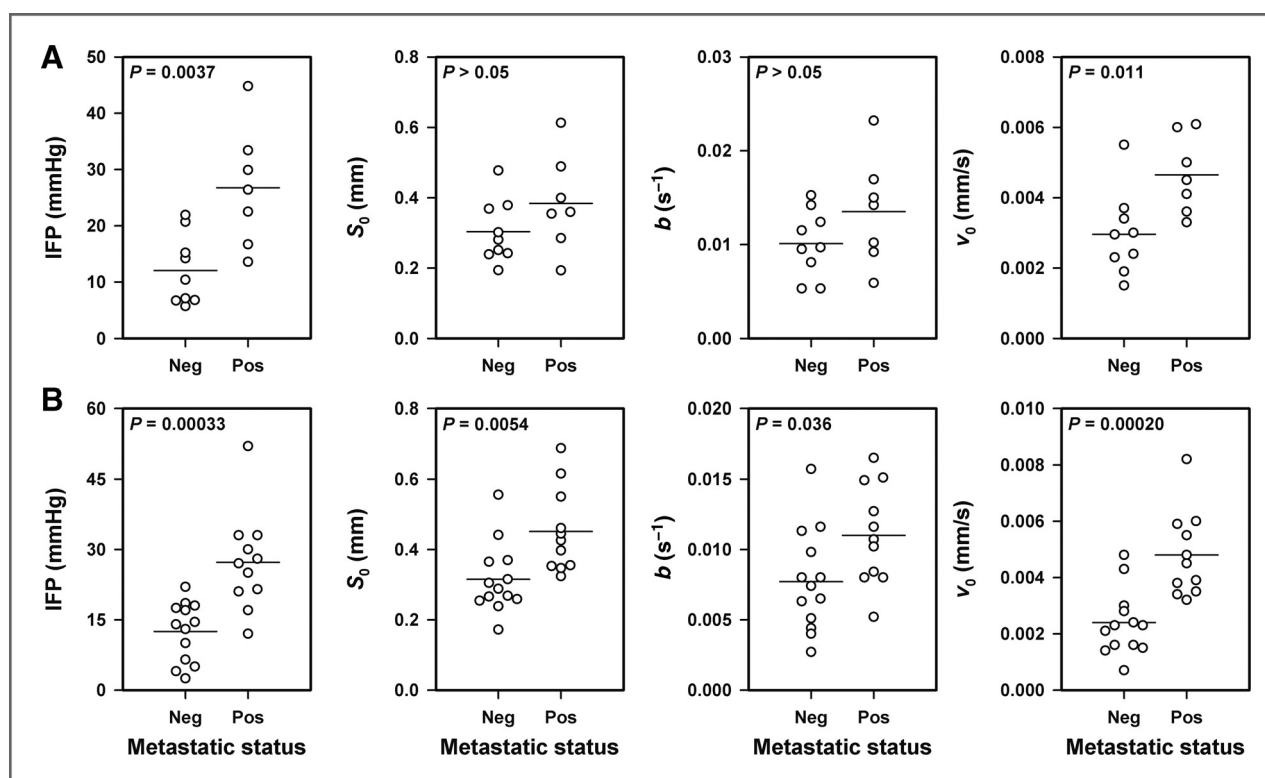


Figure 6. IFP,  $S_0$ ,  $b$ , and  $v_0$  of nonmetastatic (Neg) and metastatic (Pos) TS-415 tumors (A) and U-25 tumors (B). Symbols represent single tumors. Horizontal lines show mean values.  $P$  values were determined by the Student  $t$  test or the Mann-Whitney rank-sum test. Neg, negative; Pos, positive; s, seconds.

## Discussion

A novel noninvasive DCE-MRI technique for assessing the IFP of human and experimental tumors is reported in the present communication. The technique is based on measurements of the movement of a high-signal-intensity rim in the tumor periphery and a model for peritumoral interstitial fluid flow. The velocity of Gd-DTPA in the tumor periphery is assumed to be equal to the fluid flow velocity, and this assumption is reasonable because Gd-DTPA does not interact with the extracellular matrix (30). Our model for peritumoral interstitial fluid flow appeared to be valid because plots of  $S$  versus  $t$  were well fitted by  $S(t) = S_0 \cdot (1 - e^{-bt})$ , both for xenografted tumors and human cervical carcinomas.

Three parameters ( $S_0$ ,  $b$ , and  $v_0$ ) were calculated from the DCE-MRI data, and these parameters are related to each other through  $v_0 = S_0 \cdot b$ . Their numerical values are determined by several properties of the tumor and the surrounding normal tissue, primarily the IFP of the tumor, the hydraulic conductivity of the surrounding normal tissue, and the density and functionality of the peritumoral lymphatics. The correlation between  $v_0$  and IFP was stronger than the correlation between  $S_0$  and IFP and the correlation between  $b$  and IFP, both in TS-415 and U-25 tumors. Moreover, in contrast to  $S_0$  and  $b$ ,  $v_0$  did not vary around the tumor periphery. Consequently, the IFP of the tumors was described better by  $v_0$  than by  $S_0$  and  $b$ .

In addition,  $v_0$  discriminated better between metastatic and nonmetastatic tumors than did  $S_0$  and  $b$ . Thus, in contrast to  $S_0$  and  $b$ ,  $v_0$  was significantly higher for the tumors that had

metastasized than for those that had not metastasized, regardless of whether TS-415 and U-25 xenografts or human cervical carcinomas were considered. Taken together, our observations suggest that  $v_0$  may be a useful surrogate parameter for interstitial hypertension-induced tumor aggressiveness.

However, as mentioned above,  $v_0$  is not determined solely by the IFP of a tumor, but is also influenced by features of the surrounding normal tissue, implying that any relationship between  $v_0$  and IFP is expected to differ with the organ in which the tumors are growing. In our work, the TS-415 cervical carcinomas and the U-25 melanomas were transplanted intramuscularly, and nearly identical correlations between  $v_0$  and IFP were found for these lines. On the other hand, the  $v_0$  values measured for the human cervical carcinomas were substantially higher than those measured for the xenografted tumors, and this difference in  $v_0$  can probably not be attributed to a difference in IFP because the IFP values measured in the TS-415 and U-25 tumors were within the same range as those measured in locally advanced cervical carcinomas in humans by Milosevic and colleagues (12) and Yeo and colleagues (13). Consequently, assessment of tumor IFP and interstitial hypertension-induced tumor aggressiveness from measurements of  $v_0$  requires tumor site-specific translational criteria.

Correct assessment of  $v_0$  requires that the tumor does not move during the image acquisition. Tumor movements can be easily avoided and/or monitored in the experimental setting. In the present work, the TS-415 and U-25 tumors were transplanted into the gastrocnemius muscle to avoid breathing

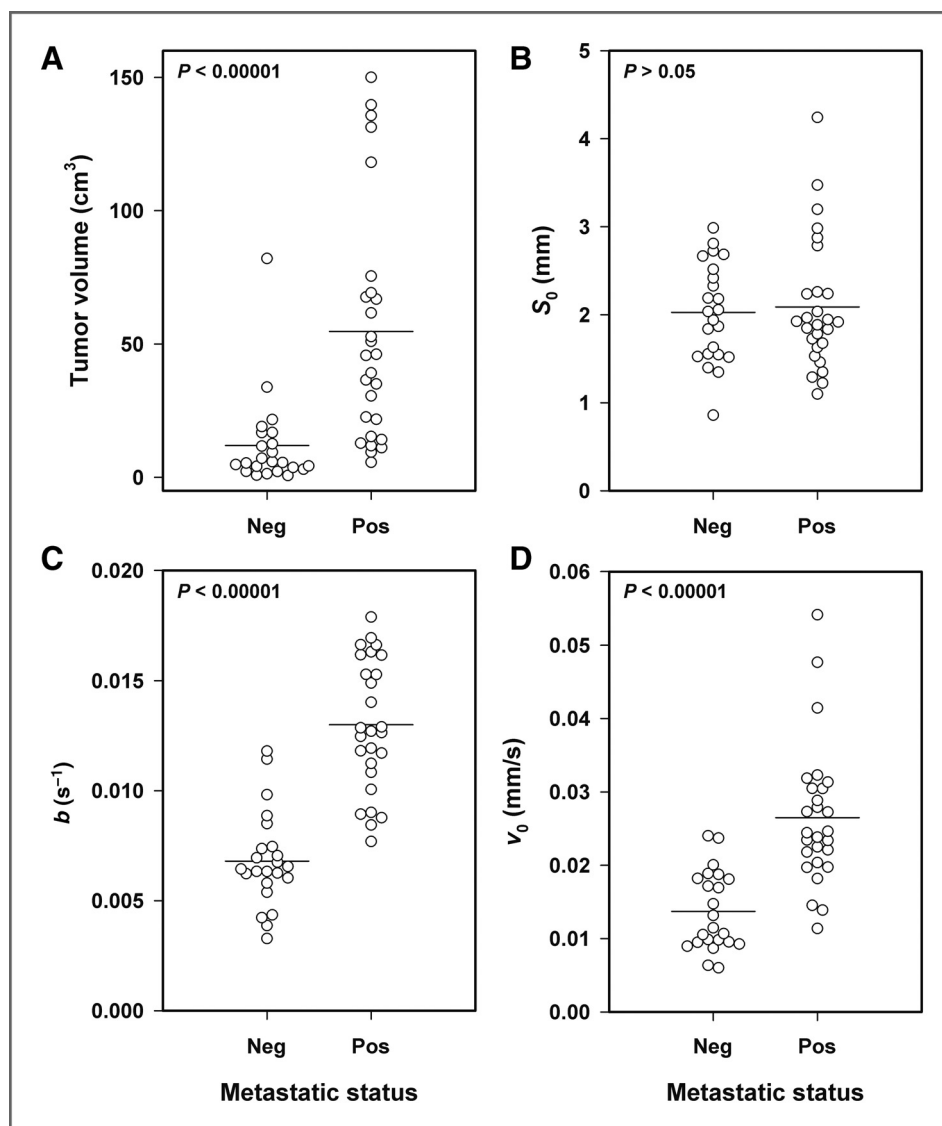


Figure 7. Volume (A),  $S_0$  (B),  $b$  (C), and  $v_0$  (D) of nonmetastatic (Neg) and metastatic (Pos) locally advanced squamous cell cervical carcinomas. Symbols represent individual patients. Horizontal lines show mean values.  $P$  values were determined by the Student  $t$  test or the Mann-Whitney rank-sum test. Neg, negative; Pos, positive; s, seconds.

artifacts during the imaging. Furthermore, the tumor-bearing leg was fixed with tape. To verify that the tumors did not move, the tumor position relative to the image matrix was examined. On the other hand, tumor movement may be a problem in the clinical setting, particularly for tumors in the pelvis where bowel and bladder movements may cause image distortions. However, this problem may be reduced by purging the patients before the MR examination.

Measurement of  $v_0$  by DCE-MRI presupposes that a high-signal-intensity rim can be detected in the tumor periphery shortly after the administration of Gd-DTPA. A high-signal-intensity peritumoral rim in Gd-DTPA-enhanced  $T_1$ -weighted images probably requires that the tumor has higher microvascular density in the periphery than in the central regions as well as high vessel wall permeability to Gd-DTPA. Gd-DTPA has a low molecular weight of 0.55 kDa and is therefore readily transported across the vessel wall of tumors. Interestingly, all TS-415 and all U-25 tumors showed a signal enhancement

pattern such as the one illustrated in Fig. 2B. Furthermore, all cervical carcinoma patients had tumors displaying an adequate early high-signal-intensity peritumoral rim. This is not necessarily a general phenomenon, implying that our DCE-MRI method for assessing interstitial hypertension-induced tumor aggressiveness may not be applicable to all tumor types. However, quantitative histologic studies involving a large number of tumor types have revealed that tumors typically show a particularly high density of microvessels and vascular hot spots in the invasive front (31–33). Moreover, a high-signal-intensity peritumoral rim has been observed in contrast-enhanced  $T_1$ -weighted images of primary tumors and liver metastases of several histologic types (34–38).

Measurement of  $v_0$  also requires that the high-signal-intensity rim is detectable for a period of 5 to 10 minutes and that the position of the rim is not influenced significantly by factors other than the peritumoral fluid flow velocity. Differing initial signal intensities caused by differences in tumor size and

decreases in signal intensity caused by peritumoral clearance of Gd-DTPA or Gd-DTPA diffusion are conceivable confounding factors. However, we present solid evidence that these factors do not represent a serious problem. Thus, significant correlations between tumor size and  $\nu_0$  or IFP were not found, and the correlations between  $\nu_0$  and IFP found for Gd-DTPA were similar to those found for gadomelitol in both tumor lines. The plasma clearance rate of gadomelitol is less than half of that of Gd-DTPA (39), and gadomelitol has a diffusion coefficient in water that is only 20% to 25% of that of Gd-DTPA (40). However, gadomelitol is not superior to Gd-DTPA for assessment of  $\nu_0$  because of the lower vessel wall permeability to gadomelitol.

The interstitial transport in tumors of small molecules such as Gd-DTPA is driven by a combination of diffusion and convection (3, 5). Diffusion is the dominant mechanism in the central regions of experimental tumors where the IFP is uniformly elevated. There is evidence from theoretical studies that diffusion may be an important mechanism even in the peripheral zone (41, 42). However, the present study showed clearly that convection is the dominant transport mechanism for Gd-DTPA in the tumor periphery. Our observations are consistent with data reported by Hassid and colleagues (15). They administered Gd-DTPA slowly to tumor-bearing mice and showed that the steady-state concentration of Gd-DTPA was high in the tumor center and decreased steeply at the tumor surface, an observation that led them to conclude that Gd-DTPA is transported primarily by convection in the periphery of tumors with high IFP.

There are several possible mechanisms for a link between  $\nu_0$  and lymph node metastasis. It has been suggested that the fluid flow from a tumor into the surrounding normal tissue may direct tumor cells toward functional peritumoral lymphatics by autologous chemotaxis, and proteolytic enzymes and chemokines carried by the interstitial fluid may facilitate tumor cell migration by remodeling the extracellular matrix (43). Furthermore, lymphangiogenic factors transported by the interstitial fluid may promote lymph node metastasis and metastatic growth by dilating peritumoral lymphatics and inducing sinusoidal hyperplasia and lymphangiogenesis in the

sentinel lymph node (44, 45). There is also some evidence that the tumor-draining lymph node may be an immune-privileged site for metastatic growth because increased interstitial and lymphatic fluid flow may alter the host immunity to tumor cells (45).

In summary, positive correlations were found between  $\nu_0$  and IFP in cervical carcinoma and melanoma xenografts, and xenografted tumors that developed lymph node metastases showed higher  $\nu_0$  and higher IFP than those that did not metastasize. Moreover, the  $\nu_0$  of the primary tumor discriminated clearly between cervical cancer patients with and without metastatic growth in pelvic lymph nodes. These observations suggest that high IFP in tumors may promote lymph node metastasis and that Gd-DTPA-based DCE-MRI may provide valid information on the IFP of tumors. The possibility that  $\nu_0$  may be an important biomarker for interstitial hypertension-induced cancer aggressiveness merits comprehensive clinical investigations.

#### Disclosure of Potential Conflicts of Interest

No potential conflicts of interest were disclosed.

#### Authors' Contributions

**Conception and design:** T. Hompland, C. Ellingsen, K.M. Øvrebø, E.K. Rofstad  
**Development of methodology:** T. Hompland, E.K. Rofstad  
**Acquisition of data (provided animals, acquired and managed patients, provided facilities, etc.):** T. Hompland, C. Ellingsen, K.M. Øvrebø,  
**Analysis and interpretation of data (e.g., statistical analysis, biostatistics, computational analysis):** T. Hompland, E.K. Rofstad  
**Writing, review, and/or revision of the manuscript:** T. Hompland, C. Ellingsen, K.M. Øvrebø, E.K. Rofstad  
**Administrative, technical, or material support (i.e., reporting or organizing data, constructing databases):** T. Hompland, C. Ellingsen, K.M. Øvrebø, E.K. Rofstad  
**Study supervision:** E.K. Rofstad

#### Grant Support

Financial support was received from the Norwegian Cancer Society and the South-Eastern Norway Regional Health Authority.

The costs of publication of this article were defrayed in part by the payment of page charges. This article must therefore be hereby marked *advertisement* in accordance with 18 U.S.C. Section 1734 solely to indicate this fact.

Received March 12, 2012; revised July 26, 2012; accepted July 27, 2012; published online October 1, 2012.

#### References

- Lunt SJ, Fyles A, Hill RP, Milosevic M. Interstitial fluid pressure in tumors: therapeutic barrier and biomarker of angiogenesis. *Future Oncol* 2008;4:793–802.
- Heldin CH, Rubin K, Pietras K, Östman A. High interstitial fluid pressure—an obstacle in cancer therapy. *Nat Rev Cancer* 2004;4:806–13.
- Jain RK. Delivery of molecular medicine to solid tumors. *Science* 1996;271:1079–80.
- Boucher Y, Jain RK. Microvascular pressure is the principal driving force for interstitial hypertension in solid tumors: implications for vascular collapse. *Cancer Res* 1992;52:5110–4.
- Boucher Y, Baxter LT, Jain RK. Interstitial pressure gradients in tissue-isolated and subcutaneous tumors: implications for therapy. *Cancer Res* 1990;50:4478–84.
- Eikenes L, Bruland ØS, Brekken C, de Lange Davies C. Collagenase increases the transcapillary gradient and improves the uptake and distribution of monoclonal antibodies in human osteosarcoma xenografts. *Cancer Res* 2004;64:4768–73.
- Jain RK. Delivery of novel therapeutic agents in tumors: physiological barriers and strategies. *J Natl Cancer Inst* 1989;81:570–6.
- Rofstad EK, Gaustad JV, Brurberg KG, Mathiesen B, Galappathi K, Simonsen TG. Radiocurability is associated with interstitial fluid pressure in human tumor xenografts. *Neoplasia* 2009;11:1243–51.
- Rofstad EK, Ruud EBM, Mathiesen B, Galappathi K. Associations between radiocurability and interstitial fluid pressure in human tumor xenografts without hypoxic tissue. *Clin Cancer Res* 2010;16:936–45.
- Rofstad EK, Tunheim SH, Mathiesen B, Graff BA, Halsør EF, Nilsen K, et al. Pulmonary and lymph node metastasis is associated with primary tumor interstitial fluid pressure in human melanoma xenografts. *Cancer Res* 2002;62:661–4.
- Ellingsen C, Hompland T, Mathiesen B, Rofstad EK. Microenvironment-associated lymph node metastasis of human cervical carcinoma xenografts. *Acta Oncol* 2012;51:465–72.
- Milosevic M, Fyles A, Hedley D, Pintilie M, Levin W, Manchul L, et al. Interstitial fluid pressure predicts survival in patients with cervix cancer

- independent of clinical prognostic factors and tumor oxygen measurements. *Cancer Res* 2001;61:6400–5.
13. Yeo SG, Kim JS, Cho MJ, Kim KH, Kim JS. Interstitial fluid pressure as a prognostic factor in cervical cancer following radiation therapy. *Clin Cancer Res* 2009;15:6201–7.
  14. Fyles A, Milosevic M, Pintilie M, Syed A, Levin W, Manchul L, et al. Long-term performance of interstitial fluid pressure and hypoxia as prognostic factors in cervix cancer. *Radiother Oncol* 2006;80:132–7.
  15. Hassid Y, Furman-Haran E, Margalit R, Eilam R, Degani H. Noninvasive magnetic resonance imaging of transport and interstitial fluid pressure in ectopic human lung tumors. *Cancer Res* 2006;66:4159–66.
  16. Gulliksrud K, Brurberg KG, Rofstad EK. Dynamic contrast-enhanced magnetic resonance imaging of tumor interstitial fluid pressure. *Radiother Oncol* 2009;91:107–13.
  17. Gulliksrud K, Galappathi K, Rofstad EK. Interstitial fluid pressure and vascularity of intradermal and intramuscular human tumor xenografts. *Int J Radiat Oncol Biol Phys* 2011;80:258–64.
  18. Haider MA, Sitartchouk I, Roberts TPL, Fyles A, Hashmi AT, Milosevic M. Correlations between dynamic contrast-enhanced magnetic resonance imaging-derived measures of tumor microvasculature and interstitial fluid pressure in patients with cervical cancer. *J Magn Reson Imaging* 2007;25:153–9.
  19. Liu LJ, Brown SL, Ewing JR, Schlesinger M. Phenomenological model of interstitial fluid pressure in a solid tumor. *Phys Rev E Stat Nonlin Soft Matter Phys* 2011;84 (2 Pt 1):021919.
  20. Jain RK, Tong RT, Munn LL. Effect of vascular normalization by antiangiogenic therapy on interstitial hypertension, peritumor edema, and lymphatic metastasis: insights from a mathematical model. *Cancer Res* 2007;67:2729–35.
  21. Shields JD, Fleury ME, Yong C, Tomei AA, Randolph GJ, Swartz MA. Autologous chemotaxis as a mechanism of tumor cell homing to lymphatics via interstitial flow and autocrine CCR7 signaling. *Cancer Cell* 2007;11:526–38.
  22. Ellingsen C, Natvig I, Gaustad JV, Gulliksrud K, Egeland TAM, Rofstad EK. Human cervical carcinoma xenograft models for studies of the physiological microenvironment of tumors. *J Cancer Res Clin Oncol* 2009;135:1177–84.
  23. Rofstad EK, Mathiesen B. Metastasis in melanoma xenografts is associated with tumor microvascular density rather than extent of hypoxia. *Neoplasia* 2010;12:889–98.
  24. Benjaminsen IC, Graff BA, Brurberg KG, Rofstad EK. Assessment of tumor blood perfusion by high-resolution dynamic contrast-enhanced MRI: a preclinical study of human melanoma xenografts. *Magn Reson Med* 2004;52:269–76.
  25. Egeland TAM, Gaustad JV, Vestvik IK, Benjaminsen IC, Mathiesen B, Rofstad EK. Assessment of fraction of radiobiologically hypoxic cells in human melanoma xenografts by dynamic contrast-enhanced MRI. *Magn Reson Med* 2006;55:874–82.
  26. Ozerdem U, Hargens AR. A simple method for measuring interstitial fluid pressure in cancer tissues. *Microvasc Res* 2005;70:116–20.
  27. Rofstad EK, Galappathi K, Mathiesen B, Ruud EBM. Fluctuating and diffusion-limited hypoxia in hypoxia-induced metastasis. *Clin Cancer Res* 2007;13:1971–8.
  28. Rosset A, Spadola L, Ratib O. OsiriX: an open-source software for navigating in multidimensional DICOM images. *J Digit Imaging* 2004;17:205–16.
  29. Rofstad EK, Halsør EF. Hypoxia-associated spontaneous pulmonary metastasis in human melanoma xenografts: involvement of microvascular hot spots induced in hypoxic foci by interleukin 8. *Br J Cancer* 2002;86:301–8.
  30. Reddy ST, Berk DA, Jain RK, Swartz MA. A sensitive *in vivo* model for quantifying interstitial convective transport of injected macromolecules and nanoparticles. *J Appl Physiol* 2006;101:1162–9.
  31. Weidner N. Intratumor microvessel density as a prognostic factor in cancer. *Am J Pathol* 1995;147:9–18.
  32. Vermeulen PB, Gasparini G, Fox SB, Toi M, Martin L, McCulloch P, et al. Quantification of angiogenesis in solid human tumours: an international consensus on the methodology and criteria of evaluation. *Eur J Cancer* 1996;32A:2474–84.
  33. Hasan J, Byers R, Jayson GC. Intra-tumoural microvessel density in human solid tumours. *Br J Cancer* 2002;86:1566–77.
  34. Kobayashi M, Kawashima H, Matsui O, Zen Y, Suzuki M, Inokuchi M, et al. Two different types of ring-like enhancement on dynamic MR imaging in breast cancer: correlation with the histopathologic findings. *J Magn Reson Imaging* 2008;28:1435–43.
  35. Uematsu T, Kasami M, Nicholson BT. Rim-enhancing breast masses with smooth or spiculated margins on magnetic resonance imaging: histopathology and clinical significance. *Jpn J Radiol* 2011;29:609–14.
  36. Tsuda K, Murakami T, Kurachi H, Ogawa H, Oi H, Miyake A, et al. MR imaging of cervical carcinoma: comparison among T2-weighted, dynamic, and postcontrast T1-weighted images with histopathological correlation. *Abdom Imaging* 1997;22:103–7.
  37. Zhang BY, Chen H, Geng DY, Yin B, Li YX, Zhong P, et al. Computed tomography and magnetic resonance features of gliosarcoma: a study of 54 cases. *J Comput Assist Tomogr* 2011;35:667–73.
  38. Yu JS, Rofsky NM. Hepatic metastases: perilesional enhancement on dynamic MRI. *AJR Am J Roentgenol* 2006;186:1051–8.
  39. Gulliksrud K, Hompland T, Galappathi K, Rofstad EK. Assessment of tumor hypoxia and interstitial fluid pressure by gadomelitol-based dynamic contrast-enhanced magnetic resonance imaging. *Radiother Oncol* 2011;101:217–22.
  40. Mescam M, Eliat PA, Fauvel C, de Certaines JD, Bezy-Wendling J. A physiologically based pharmacokinetic model of vascular-extravascular exchanges during liver carcinogenesis: application to MRI contrast agents. *Contrast Media Mol Imaging* 2007;2:215–28.
  41. Swabb EA, Wei J, Gullino PM. Diffusion and convection in normal and neoplastic tissues. *Cancer Res* 1974;34:2814–22.
  42. Jain RK. Transport of molecules in the tumor interstitium: a review. *Cancer Res* 1987;47:3039–51.
  43. Rutkowski JM, Swartz MA. A driving force for change: interstitial flow as a morphoregulator. *Trends Cell Biol* 2007;17:44–50.
  44. Mumprecht V, Detmar M. Lymphangiogenesis and cancer metastasis. *J Cell Mol Med* 2009;13:1405–16.
  45. Swartz MA, Lund AW. Lymphatic and interstitial flow in the tumour microenvironment: linking mechanobiology with immunity. *Nature Rev Cancer* 2012;12:210–9.